Planetary and Space Science 81 (2013) 18–31

Contents lists available at SciVerse ScienceDirect

Planetary and Space Science

journal homepage: www.elsevier.com/locate/pss

On the possibility of lunar core phase detection using new seismometers for soft-landers in future lunar missions

Ryuhei Yamada [a,b,c,d,*], Raphael F. Garcia [c,d], Philippe Lognonné [e], Naoki Kobayashi [b], Nozomu Takeuchi [f], Tanguy Nébut [e], Hiroaki Shiraishi [b], Marie Calvet [c,d], J. Ganepain-Beyneix [e]

[a] National Astronomical Observatory of Japan, RISE Project 2-21-1 Osawa, Mitaka, Tokyo 181-8588, Japan
[b] Institute of Space and Astronautical Science, Japan Aerospace Exploration Agency, 3-1-1 Yoshinodai, Sagamihara, Kanagawa 229-8510, Japan
[c] Université de Toulouse, UPS-OMP, IRAP, Toulouse, France
[d] CNRS, IRAP 14, Avenue Edouard Belin, F-31400 Toulouse, France
[e] Equipe Géophysique Spatiale et Planétaire, Institut de Physique du Globe du Paris, Sorbonne Paris Cité, Université Paris Diderot, UMR 7154 CNRS, F-94100 Saint Maur des Fossés, France
[f] Earthquake Research Institute, University of Tokyo, Bunkyo-ku, Tokyo 113-0032, Japan

ARTICLE INFO

Article history:
Received 11 June 2012
Received in revised form
28 February 2013
Accepted 22 March 2013
Available online 3 April 2013

Keywords:
Seismometer
Planetary exploration
Lunar exploration
Moonquake
Lunar seismicity
Lunar core

ABSTRACT

Information on the lunar central core; size, current state and composition; are key parameters to understand the origin and evolution of the Moon. Recent studies have indicated that possible seismic energies of core-reflected phases can be identified from past Apollo seismic data, and core sizes are determined, but we have still uncertainties to establish the lunar core parameters. We, therefore, plan to detect seismic phases that pass through the interior of the core and/or those reflected from the core–mantle boundary to ensure the parameters using new seismometers for future lunar soft-landing missions such as SELENE-2 and Farside Explorer projects.

As the new seismometers, we can apply two types of sensors already developed; they are the Very Broad Band (VBB) seismometer and Short Period (SP) seismometer. We first demonstrate through waveform simulations that the new seismometers are able to record the lunar seismic events with S/N much better than Apollo seismometers. Then, expected detection numbers of core-phases on the entire lunar surface for the two types of seismometers are evaluated for two models of seismic moment distributions of deep moonquakes using the recent interior model (VPREMOON).

The evaluation indicates that the VBB has performance to detect reflected S phases (ScS) from the core–mantle boundary mainly on the lunar near-side, and the P phases (PKP) passing through the interior of the core on some areas of the lunar far-side. Then, the SP can also detect PKP phases as first arrival seismic phase on limited regions on the lunar far-side. If appropriate positions of the seismic stations are selected, core-phases can be detected, allowing us to constrain the origin and evolution of the Moon with future lunar soft-landing missions.

1. Introduction

The information about interior structures of planetary bodies is a key parameter to understand the process of differentiation and the original materials of the bodies. Though the first lunar seismological experiments during NASA Apollo programs have provided much information about lunar interior structure and lunar seismic activities (Nakamura et al., 1982; Lognonné et al., 2003), we still have difficulties in revealing the lunar deep structure, including the lunar core due to the regional geometry of four Apollo seismic stations (Apollo 12 and 14–16) on the lunar near-side, and limited frequency responses and sensitivities of Apollo seismometers.

Early studies based on Lunar prospector data or Apollo Lunar reflectors have suggested that the Moon has a small metallic and conductive core (Hood et al., 1999), likely liquid (Williams et al., 2001). We have to know its size and density to estimate the total amount of siderophile elements in the Moon so as to validate the Moon's formation through a giant impact scenario (Canup and Asphaug, 2001), and constrain the temperature of the mantle (Gagnepain-Beyneix et al., 2006; Khan et al., 2006) to understand the thermal history of the Moon.

Recent studies (Weber et al., 2011; Garcia et al., 2011) have indicated that they could identify the energies of seismic phases reflected from the core–mantle boundary using the technique of

* Corresponding author at: National Astronomical Observatory of Japan, RISE Project, Center Building (South area) 209 2-21-1, Osawa Mitaka, Tokyo 181-8588, Japan. Tel.: +81 422 34 3940; fax: +81 422 34 3596.
E-mail address: ryamada@miz.nao.ac.jp (R. Yamada).

0032-0633/$ - see front matter © 2013 Elsevier Ltd. All rights reserved.
http://dx.doi.org/10.1016/j.pss.2013.03.009

waveform stacking of deep moonquake events, which occur repeatedly on a specific nest located at the lunar deep region between depths of about 700 and 1200 km, related with positions of the Earth, the Moon and the Sun; that is tidal forcing (Lammlein, 1977), and they constrained the core size and its structure. Despite these recent core size and density estimates (Weber et al., 2011; Garcia et al., 2011), we have large uncertainties about state and composition of the lunar core because there is trade-off between the weakly constrained lower mantle and core size remains for reflected phase on their analysis and it increases uncertainty of the core radius. We do not have any direct information about state, composition and interior structure of the core because seismic phases which pass through interior of the core are not certainly identified from past Apollo data. Though Sellers (1992) described that he could identify the PKP phase (P waveform passing through interior of the core) from far-side impact data, the identification is considered to be doubtful and not definitive (Wieczorek et al., 2006). We have to certainly detect the waveforms that pass through interior of the core and those reflected from the core–mantle boundary to reduce the current error bars. That is why direct detection of core phases originated from the deep nests will be one of main topics in future lunar seismological experiments.

Currently, lunar seismological experiment, such as SELENE-2 (Tanaka et al., 2008) is planned by JAXA, and several proposals have been also made, such as the LUNETTE discovery concept (Neal et al., 2010) or the European Medium class Farside Explorer concept (Mimoun et al., 2011), and they might be re-proposed to future opportunities. In these missions, the deployment of 1 (for SELENE-2) to several seismic stations using soft-landers is planned, with a seismometer carried by the lander and deployed on the surface by a robotic arm. The Very Broad-Band seismometer (VBB) (Lognonné et al., 2000) developed at the Institut du Physique du Globe du Paris (IPGP) for previous Mars projects (Lognonné et al., 1996, 2000) and Short-Period seismometer (SP) (Yamada et al., 2009) developed in Japan Aerospace Exploration Agency (JAXA) originally for the LUNAR-A project (Mizutani et al., 2003) are considered for these projects.

In this paper, we investigate how the performances of these instruments will map in term of core phases detection, by using the expected amplitude of signals originating from the deep nests. This will enable us to confirm that reliable evidence of the lunar core can be obtained by future lunar missions. We first describe current performances (frequency responses and detection limits) of the VBB and the SP seismometers (Section 2). Then, we describe conditions of detection of the core phases by the two types of seismometers (Section 3). In Section 4, lunar interior models and seismic moments of deep events are described to estimate amplitudes of the core phases. Then, we evaluate the expected detection numbers of core-phases on each station position during an observation term (Section 5) following the conditions described in Section 3 and distributions of seismic moments of deep events estimated in Section 4. We then make some suggestions about the landing positions in future seismological missions. Finally, we discuss some agendas in this evaluation (Section 6), and conclude this topic.

2. Performances of the seismometers in future lunar soft-landing missions

2.1. Descriptions of the seismometers

We investigate two seismometers, (the VBB and the SP) described in the previous section, as candidate for future lunar soft-landing missions. These seismometers had been already developed through past planetary missions and have a high maturity. The performances were once examined and guaranteed, and the costs for application to a mission are not more expensive compared with that for development of new sensors.

2.1.1. Very broad-band seismometer

The Very Broad-Band (VBB) seismometer was originally developed for Mars missions such as the InterMarsnet and Net Lander mission (Lognonné et al., 1996, 2000), ExoMars (ESA) and INSIGHT (JPL). The VBB seismometer is a 3-axis inverted pendulum linked to its support structure through a pivot and a spring (Fig. 1). The displacement of the mobile part is monitored with a differential capacitive transducer: two electrodes are mounted on the mobile part and two electrodes on the fixed part. The relative movement of the fixed and mobile parts generates a variation of capacitor which is converted into a voltage. For each axis, this capacitor transducer drives an analog feedback electronics which then drives a magnetic actuator to generate a counter-reaction force on the pendulum. Parameters of feedback are used to tune the transfer function and the instrument self-noise as well. For Moon or Mars tuning, the instrument has an output proportional to ground velocity in the [0.02–2.0 Hz] bandwidth, while another output is proportional to the ground acceleration below 0.02 Hz. Depending on the scientific goals and requirements of the mission, both bandwidth and self-noise can be adjusted.

For use on the lunar surface instead of Mars, signal to noise ratio of the sensor must be increased by a factor of ten to detect the small lunar seismic events on the lunar surface. Three main improvements have been performed in order to achieve this goal. The first is an attachment of additional counter mass correcting for the difference of gravities between Mars (3.71 m/s^2) and the Moon (1.71 m/s^2) (Fig. 1). The second is a modification of differential capacitive sensor geometry with both a reduction of electrode's gap and increase of electrode's size to increase the sensitivity. The third is the addition of thermal compensator device to the pendulum. The purpose is to correct the center of mass displacement related to thermal variation on lunar surface. Due to absence of atmosphere on lunar surface, the very large thermal variation from −200 to +100 °C occurs during a lunar day. Since this variation is too large, SELENE-2 mission is planning to use a lunar survival module (Ogawa et al., 2010). This system covers the scientific instruments by a heat insulating shell on lunar surface, and thermal variation reduces to about 50 °C (−10 °C to+40 °C) in the shell. The thermal compensator can reduce the thermal sensitivity of the pendulum by a factor greater than 10, and the VBB will operate as designed in lunar environment using the survival module.

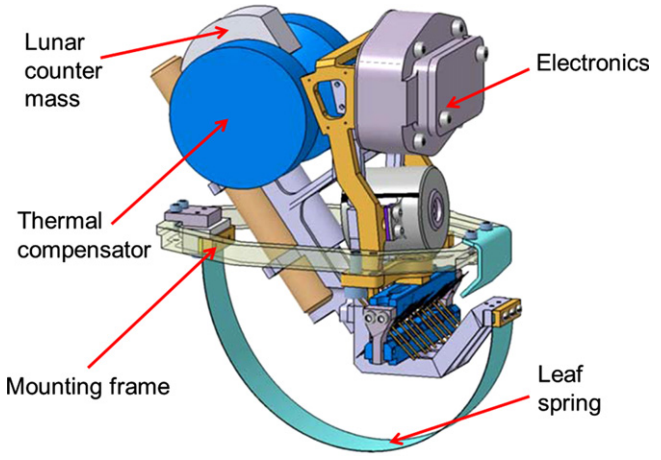

Fig. 1. Sensor head of the Very Broad Band (VBB) seismometer. This sensor head acts as pendulum of the seismometer.

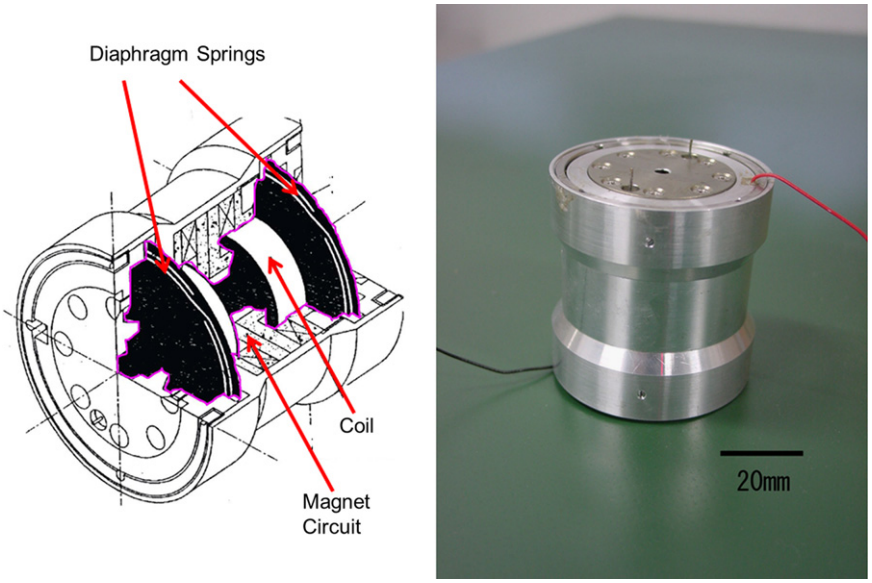

Fig. 2. Bird-eye view (left) and the photograph of the Short Period (SP) seismometer (right).

2.1.2. Short-period seismometer

The Short-Period (SP) seismometer is an electromagnetic one which has a pendulum consisting of coil and magnet circuits fixed with the case (Fig. 2). The sensor is a passive type, and do not need any electrical power for the sensor. The SP was developed through the past LUNAR-A penetrator mission (Mizutani et al., 2003). The sensor has a high-shock capability which can survive through penetrating acceleration over 10^5 m/s^2 and the performances allowing detect small deep moonquakes after the penetration (Yamada et al., 2009).

When we deploy the SP sensor on the lunar surface by a soft-lander not a penetrator, thermal variation around the sensor will be larger than for penetrator option, even if we use the survival module described above. We have already investigated the change of the performance of the SP in this new thermal range as shown in figure 6 in Yamada et al. (2009). Through the investigation, we can expect that the change of neutral position will be able to be corrected using a typical gimbal mechanism in the survival module.

In contrary to the LUNAR-A design using a pressurized atmosphere inside the penetrator, SELENE-2 surface package will deploy a sensor under vacuum on lunar surface. The variation of pressure around the seismometer can change the damping constant and the noise level (Brown noise) (Rodgers, 1992) of the sensor. We have investigated the frequency response as function of pressure, and have found the damping constant due to air friction is much smaller under pressure lower than 1 Pa than the other source of damping (e.g., Foucault currents due to the coil/magnet interaction) (Yamada et al., 2010). Under vacuum on the lunar surface, the seismometer will have only electrical damping and the value is about 0.4, in contrary to the 0.65 nominal damping constant of LUNAR-A. The performances required for lunar seismic observation are obtained under vacuum.

2.2. Frequency responses and detection limits.

The characteristics of the VBB and the SP sensors for a soft-lander are presented in Table 1. These performances include characteristics of amplifiers and filters attached to the seismometers planned for a SELENE-2 soft-lander. Fig. 3 shows the frequency responses of the VBB, the SP and the past Apollo seismometers (Long-period (A-LP) and Short-period (A-SP) sensors) (Latham et al., 1973) in units of DU/m/s. The responses of the VBB and the SP are assumed to be those at ordinary temperature and under vacuum. For future lunar missions, we plan to use 24-bits A/D converter that has much better resolution

Table 1
Characteristics of the VBB and the SP for a soft-lander.

	VBB	SP
Type	Capacitive displacement sensor	Electromagnetic sensor
Resonant frequency	0.02 Hz	1.1 Hz
Total gain	2.0E+6 V/m/s	2.2E+4 V/m/s
Size	58 mm × 93 mm × 108 mm (sensor head size)	50 mm × 50 mm (diameter × height)
Mass	0.25 kg (sensor head mass)	0.33 kg (total sensor mass)
Frequency range	0.02–2.00 Hz	1.00–50.0 Hz

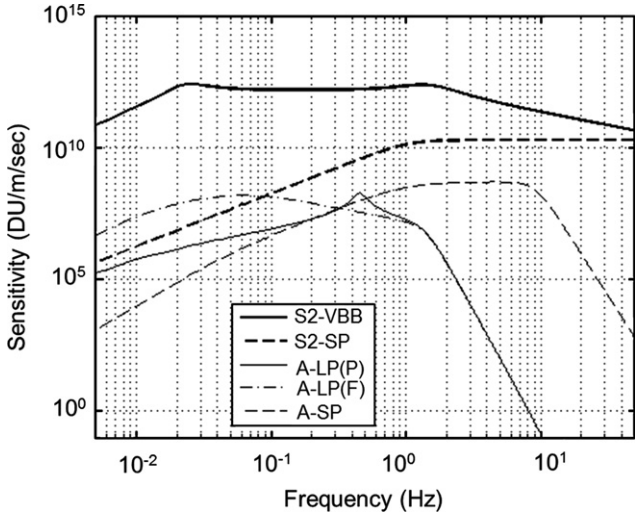

Fig. 3. Frequency responses of the new seismometers (S2-VBB and S2-SP) and the Apollo seismometers (A-LP and A-SP) for velocity. The Apollo long-period (A-LP) seismometer has two operation mode; Peaked-mode (A-LP (P)) and Flat mode (A-LP (F)) (Latham et al., 1973), and the two responses are shown in this figure.

than 10-bits A/D used in Apollo missions. Using the high-performance A/D, the sensitivity of the VBB is much higher than those of Apollo LP sensors (Fig. 3), while the self-noise of the complete VBB system is about several ten times smaller than the one of the Apollo instruments.

The detection limits of these seismometers are indicated in Fig. 4. The detection limit is defined by

$$\mathrm{Dl}(f) = \sqrt{\mathrm{NP}(f)/T(f)^2} \quad (1)$$

where Dl is the detection limit with term of velocity in $(m/s/\sqrt{Hz})$ and it is corresponding to input equivalent noise as ground motion, f is the frequency, NP is the power spectral density (PSD) of the output noise of new seismometers in V^2/Hz and T is the frequency response of the seismometer in $(V/m/s)$. The noise levels of the VBB and the SP were evaluated by the measurement and/or the theoretical equations (Yamada et al., 2009).

For the SP, the noise includes the suspension Brown noise, the transducer Johnson noise and the amplifier's one. For the VBB, this includes the capacitive transducer, the Brownian and amplifier's noise in addition to the feedback noise and the electrostatic forces, intrinsically associated to the capacitive measurement called patch effect (Kim et al., 2010). The patch effect occurs on surface of electrodes attached to the pendulum and the case. The patch due to crystal morphologies and any pollution generates the electrostatic force on the electrodes, and it may act as $1/f$ noise. The noise caused from the patch effect is inversely proportional to square of gap between electrodes (the pendulum and the case). In current status, the long-period noise level of the VBB depends therefore on patch effect amplitude and on the gaps finally chosen for the VBB. The detection limit of the VBB shown in Fig. 4 adopts a conservative case with the present design.

Note that for both the VBB and the SP, we assume that the environmental noise will be lower than the sensors self-noise, which might however request a careful installation, especially for the horizontal components, as shown by the noise level recorded on the Apollo (Lognonné and Johnson, 2007). The A/D noise, due to the 24-bit dynamics, is much smaller than both the SP and VBB noise. Possible environment noise, associated to tilt, temperature and magnetic field variations are not taken into account, but will have to be considered in the design of the sensors housing and installation.

In Fig. 4, the noise levels of the Apollo seismometers (Apollo LP (Peaked-mode) and Apollo SP) were derived from the actual seismic data by using time sequences without lunar quakes (see Lognonné and Johnson (2007) for Apollo noise level in acceleration). We assumed that the seismic data without identified lunar seismic events corresponded to the total output noise of the Apollo seismometers, as the Apollo instrument is not expecting to record the micro-seismic noise related to the continuous impacts as environment noise on the Moon (Lognonné et al., 2009). The spectra of the Apollo noise shown in Fig. 4 are derived from vertical component data of the Apollo LP and SP. Lognonné and Johnson (2007) shows that the vertical component data does not include the environment noise (horizontal noise) maybe associated to sensor tilt due to temperature variation and the noise may be related to the instrument. The noise level of the vertical component seems to represent the instrumental self-noise without environmental noise as well as those of the VBB and the SP. From comparison in Fig. 4, we can say that our seismometers have better detection limits compared to Apollo seismometers in observable frequency range (0.02–50 Hz).

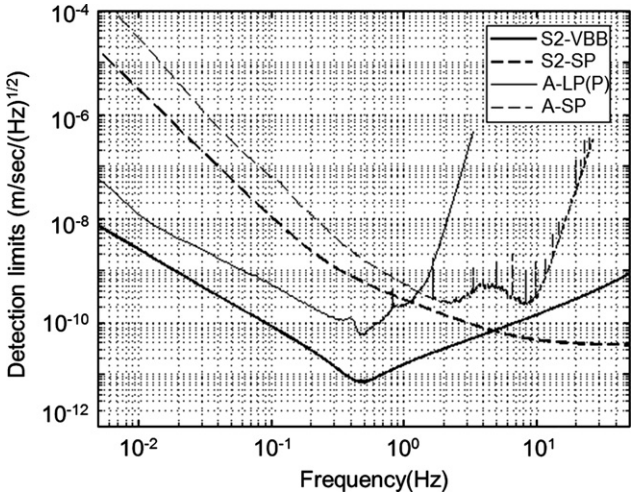

Fig. 4. Detection limits of the new seismometers and the Apollo seismometers for velocity. The detection limit of the Apollo-LP is that of Peaked-mode.

2.3. Waveform simulation of lunar seismic events

We have evaluated how the lunar seismic events can be observed by the new seismometers on the lunar surface. In this evaluation, we simulated the waveforms of the lunar seismic signals observed by the new seismometers using the past Apollo seismic data and those of noise of the sensors. The waveforms observed by the new sensors are simulated from past Apollo seismic events using the next equation:

$$\mathrm{SW}(t) = 2R_e\left[\int_0^{+\infty} \mathrm{RA}(f) \times \frac{T_n(f)}{T_a(f)} \times F(f) \times \exp(2\pi i f t) df\right] \quad (2)$$

where SW is a simulated waveform of a lunar seismic event as function of time t, RA is the Fourier spectrum of raw seismic event data observed by the Apollo seismometers, T_a and T_n are the frequency responses of the Apollo and the new (the VBB or the SP) seismometers including that of electronics, and F is the frequency response of the filter to enhance the seismic signal. R_e indicates the real part of the signal. The noise waveform of the new seismometer NW(t) also is simulated, using the next equation:

$$\mathrm{NW}(t) = 2R_e\left[\int_0^{+\infty} \sqrt{\mathrm{NS}(f)/2} \times \mathrm{RS}(f) \times F(f) \times \exp(2\pi i f t) df\right] \quad (3)$$

where RS(f) is a random phase operator and NS(f) is the single-side voltage power spectrum density of the noise of the new seismometers in V^2/Hz.

Fig. 5 shows that comparison of a deep moonquake including a noise observed by the Apollo LP with the simulated deep moonquake observed by the VBB. The waveforms are indicated in DU using characteristics of Apollo 10bit A/D or SELENE-2 24-bit A/D. From past Apollo observation, the signal to noise ratio of deep moonquake waveform is good in the 0.3–1.1 Hz frequency range. For the reason, $F(f)$ is defined as a butterworth bandpass filter with corner frequencies of 0.3 Hz and 1.1 Hz. In these figures, the small deep events which have amplitudes of about 3DU in Apollo record are compared. The noise waveform of Apollo LP (Fig.5(a)) is assumed to be pre-event data of the deep moonquake; it is signal before "Arrival of P-waveform " in the figure. This waveform is vertical component data of the LP and it seems to represent almost the instrumental self-noise without environmental noise. Here, the signal to noise ratio (S/N) can be evaluated from the event data and pre-event (noise) data in Apollo case. In the VBB case (Fig. 5(b)), the deep event simulated from Eq. (2) based on original Apollo data (3DU event) and the noise waveforms calculated from Eq. (3) are indicated. The comparison between Fig. 5(a) and (b) indicates that the VBB can detect the deep moonquake events with much better S/N and A/D resolution compared with Apollo LP seismometer, and we will be able to identify arrival of the seismic events more clearly by the VBB. Then, the signal to noise ratios of deep

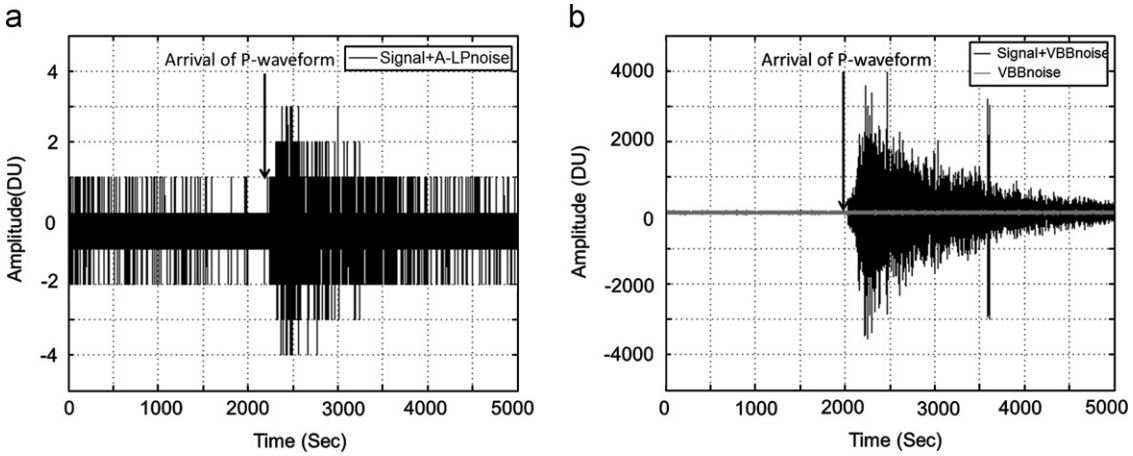

Fig. 5. Waveform of a deep moonquake originated from A1 deep nest; (a) waveform observed by the Apollo-LP seismometer (Peaked-mode), and (b) simulated waveform observed by the VBB based on Apollo deep event which have similar amplitude to that shown in (a). These waveforms are band-pass filtered between 0.3 and 1.1 Hz and de-spiked. The waveform observed by the Apollo-LP was recorded with sampling rate of 6.625 Hz and resolution of 10 bits (Apollo A/D), and the signal and noise obtained by the VBB are simulated as record with sampling rate of 100 Hz and resolution of 24 bits (SELENE-2 A/D). "Arrival of P-waveform" in these figures means that arrival of P-waveform of the deep moonquake, and in (a) the signal before the arrival corresponds to the noise of the Apollo LP seismometer system.

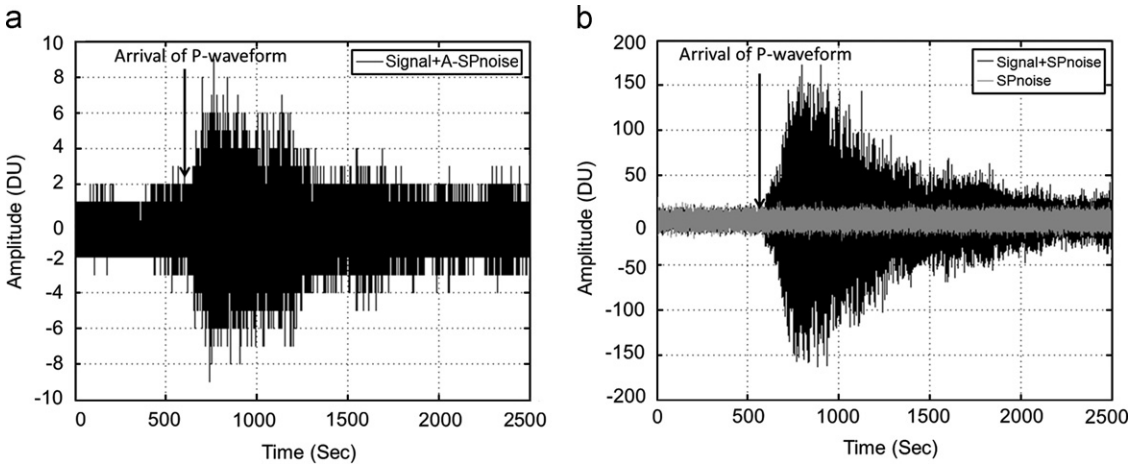

Fig. 6. Waveform of a meteoroid impact; (a) waveform observed by the Apollo-SP seismometer and (b) simulated waveform observed by the SP based on Apollo impact event which have similar amplitude to that shown in (a). These waveforms are band-pass filtered between 1.0 and 8.0 Hz and de-spiked. The waveform observed by the Apollo-SP was recorded with sampling rate of 53 Hz and resolution of 10 bits (Apollo A/D), and the signal and the noise obtained by the SP is simulated as record with sampling rate of 100 Hz and resolution of 24 bits (SELENE-2 A/D). "Arrival of P-waveform" in the figure means that arrival of P-waveform of the meteoroid impact, and in (a) the signal before the arrival corresponds to the noise of the Apollo SP seismometer system.

moonquake events observed by the VBB will be about 25 times better than those of Apollo LP between frequency range of 0.3–1.1 Hz.

The meteoroid impacts on the lunar surface are important sources to investigate the lunar shallow structure (Chenet et al., 2006). Waveforms of meteoroid impacts usually have higher frequency component compared to deep moonquakes (Duennebier and Sutton, 1974a). So, the short-period seismometer is preferred to detect the meteoroid impacts. Fig. 6 shows that the comparison of a waveform of the meteoroid impact including a noise (pre-event data) detected by the Apollo SP vertical component and that by the SELENE-2 SP between frequencies range of 1.0 and 8.0 Hz. The waveforms are also indicated in DU using characteristics of the Apollo 10-bit A/D or SELENE-2 24-bit A/D. The comparison is performed for located small meteorite impact (about 5 DU amplitudes in Apollo record). From the event, the signal to noise ratios were also evaluated in both the Apollo-SP and the SP cases as with the VBB case. This evaluation also indicates that our SP sensor on the lunar surface can detect the meteoroid impacts with better S/N and A/D resolutions compared to the Apollo-SP in this high frequency range.

The waveform simulation of the lunar seismic events observed by the new seismometers as shown in Figs. 5 and 6 indicates that we can detect more deep events and meteoroid impacts with better S/N and identify arrivals of the body waveforms more clearly than Apollo-era.

3. Evaluation method for core-phases detection

Let us now address the amplitude of core phases on single seismograms, which, in contrary to the stacked signals of Garcia et al. (2011) and Weber et al. (2011), have not been so far identified, For this purpose, we have calculated the waveforms and/or amplitudes of the core-phases of deep moonquakes using theoretical equations, possible lunar interior model and the Apollo seismic data. Then, we evaluated how many core-phases can be detected using the VBB and the SP respectively.

We have to notice effect of seismic scattering in lunar seismograms caused from heterogeneous structure of the lunar surface (Dainty et al., 1974) to estimate the waveforms of lunar core-phases.

This effect disturbs the seismic signals, and makes the waveform simulation difficult using typical theoretical equations.

On the other hand, a seismic simulation indicates that the effects of scattering will be weak for frequencies lower than about 0.1 Hz because the waves in the low frequency range have wavelength longer than thickness of the surface heterogeneous layer (Shiraishi et al., 2010). Therefore, we adopt two methods to evaluate detection of the core-phases by our seismometers for two different frequency ranges; that lower than 0.1 Hz and that higher than 0.1 Hz. We evaluate detection capability of the VBB in low frequency range and that of the SP in high frequency range.

3.1. Evaluation in low frequency range

In frequency range lower than 0.1 Hz, we can expect lunar seismograms with weak scattering effects. Though the Apollo LP sensors could not detect the seismic signals in this frequency range due to the sensor noise (Gagnepain-Beyneix et al., 2006), the better performance of the VBB in low frequency range (Fig. 4) may make us enable to detect the undisturbed waveform in the future missions. In this study, we assume that we can detect the lunar seismic signals with little scattering effects and calculate the waveform by typical theoretical equations in frequency range around 0.1 Hz.

In this case, we set the condition of detection of the core-phases as

$$U_{max} > N_R \tag{4}$$

where U_{max} is the maximum amplitude of the time-series theoretical waveform $U(t,\Delta,K)$ of seismic phase K at an epicentral distance of Δ in term of velocity, and N_R is the RMS amplitude of the noise waveform of the seismometer in terms of velocity. U is calculated using following equations (Aki and Richards, 2002):

$$U(t,\Delta,K) = 2R_e\left[\int_0^{+\infty} A_0(f,\Delta,K)\times\exp\left\{2if\left[\pi(t-T)+t^*(K)\ln\left(\frac{f}{f_s}\right)\right]\right\}\times F(f)\times\exp(-\pi f t^*(K))df\right] \tag{5}$$

$$t^*(K) = \int_Q^{dt}(K) \tag{6}$$

where T is the travel time of the seismic phase, f_s is the scaling frequency and Q is the seismic quality factor. We set the scaling frequency as 1.0 Hz. In Eq. (5), we assume that surface response is 1.0. $F(f)$ is the response of the bandpass filter to enhance the signal between a specific frequency range. $A_0(f,\Delta,K)$ is the velocity Fourier amplitude of input impulse without attenuation at frequency of f, and it is calculated as

$$A_0(f,\Delta,K) = 2\pi f\times rp(K)\times\dot{M}(f)\times S_f(K)\times R_{tc}(K)/R(\Delta) \tag{7}$$

where rp is the radiation pattern, $\dot{M}$ is the source function, and S_f is the geo-scale factor given by

$$S_f(K) = \frac{\cos(\lambda)}{4\pi\sqrt{\rho_s\rho_e\alpha_s(K)\alpha_e(K)^5}} \tag{8}$$

where ρ_s and ρ_e are the densities of the lunar surface and source region, α_s and α_e are the P or S-wave velocity of the lunar surface and source region, λ is the incident angle of the seismic phase. R_{tc} is the integrated value of reflectance and transmission coefficients through the seismic path. $R(\Delta)$ is the geometrical spreading at epicentral distance of Δ (Aki and Richards, 2002).

Though we do not have evident information about source function of moonquakes, Goins et al., (1981) estimated that the corner frequency of the deep moonquake may be about 1.0 Hz from analysis of the spectrum. Then, in this low frequency range, we can presume as

$$\dot{M}(f) = M_0 \text{ (below about 1.0 Hz)} \tag{9}$$

where M_0 is the seismic moment in Nm. We have little information about radiation patterns of moonquakes. In this study, we adopt constant value of 0.5 as the radiation pattern for all seismic phases, then $rp(K) = rp = 0.5$.

N_R in Eq. (4) is the effective (root-mean-square) value of input equivalent noise converted to ground motion (velocity) of the seismometer. The effective value is represented by the following equation, using $Dl(f)$ in Eq. (1), such that

$$N_R = \sqrt{\int Dl(f)^2 df} \tag{10}$$

Using Eqs. (4)–(10), we will evaluate the detection of the core-phases by the VBB in the low frequency range.

3.2. Evaluation in high frequency range

In the frequency range higher than about 0.1 Hz, it is difficult to predict waveforms of the core-phases using theoretical equations such as Eq. (5), due to effect of intensive scattering. Therefore, we adopt an assumption that the energy of an input impulse before scattering is preserved after the scattering on lunar surface. That means that average square amplitude of an input impulse is equivalent to that of an observed waveform whose time window is T_0 after arrival to the surface. Then, we set the condition of detection of core phases as

$$\overline{sw}^2 > \overline{nw}^2 \tag{11}$$

where $\overline{nw}^2$ is the average square amplitude of moonquake waveform, which has a time window of T_0, and $\overline{nw}^2$ is also the average square amplitude of noise waveform of the seismometer, whose time window is T_0. The average square amplitude of a seismic signal of phase K observed at an epicentral distance of Δ is defined as

$$\overline{sw}^2(\Delta,K) = \int P(f,\Delta,K)df \tag{12}$$

$$P(f,\Delta,K) = \frac{1}{T_0}\left|S(f,\Delta,K)\right|^2 \tag{13}$$

where $P(f,\Delta,K)$ and $S(f,\Delta,K)$ are PSD and Fourier amplitudes of the seismic signal of phase K observed at an epicentral distance of Δ in velocity. As described above, since the average square amplitude of the observed signal is equivalent to that of input impulse before scattering, the Fourier amplitude is represented by theoretical equation including attenuation effect;

$$S(f,\Delta,K) = A_0(f,\Delta,K)\times exp(-\pi f t^*(K)) \tag{14}$$

The average square amplitude of a noise waveform is also defined by

$$\overline{nw}^2 = N_R^2 = \int Dl(f)^2 df \tag{15}$$

This noise waveform is represented as the input equivalent noise converted to ground motion (velocity). Eq. (11) is rewritten using Eqs. (12)–(15), such that

$$\frac{1}{T_0}\int\left|A_0(f,\Delta,K)\times\exp(-\pi f t^*(K))\right|^2 df > \int Dl(f)^2 df \tag{16}$$

In this study, the frequency bandwidth [0.5–1.5 Hz] is used as high frequency range, because we can identify the seismic signals of deep moonquakes around this frequency from Apollo data at least. We also assume $\dot{M}(f) = M_0$ during this frequency range in the calculation of Eq. (14). In this bandwidth, we will take as reference the SP seismometer performance.

From Eqs. (4) and (16), we can evaluate core-phase detection in both low frequency and high frequency, if we know the values of $A_0(f, \Delta, K)$ and $t^*(K)$ of the core-phases and detection limits of the LP bandwidth of the VBB and the SP bandwidth of the SP. The detection limits are already indicated in Fig. 4. For the calculations of $A_0(f, \Delta, K)$ and $t^*(K)$ based on Eqs. (6)–(9), we need information of lunar interior structure and seismic moment which are described in the next section.

4. Models

4.1. Lunar interior model

In this study, we use the VPREMOON lunar interior model (Garcia et al., 2011). In this model, the velocity structure of mantle and crust was constructed to satisfy lunar seismic and geodetic data, and a lunar core size of 380 ± 40 km was estimated by detection of core-reflected shear wave energy; ScSH. The liquid Fe-core seems to be appropriate based on geophysical data such as magnetic data (Hood et al., 1999), geodetic data (Williams et al., 2001; Khan and Mosegaard, 2005) and the seismic data (Garcia et al., 2011). Though the P and S wave velocities and density change with depth in the mantle of VPREMOON model, we used the averages of P and S wave velocities and density as the parameters in the lunar mantle for simplification of calculation because it does not affect on values of calculated amplitudes so much and constant elastic velocity in the mantle also seems to be appropriate in other studies (Khan et al., 2006). The values of seismic quality factor were referred from Table 6 in Garcia et al., (2011).

Fig. 7 shows the lunar interior model used in this study; (a) profiles of P and S-wave, density and (b) seismic quality factor with Moon's radius. Since the value of P-wave velocity in the lunar core is not defined in the VPREMOON model, we adopted the value of 5.0 km/s from Sellers (1992). As described in Section 1, this value has large uncertainty. However, some measurements under high temperature and pressure show that the compressional wave velocity of liquid Fe is about 4.0–4.5 km/s under pressure in lunar central core (about 5 GPa) (Sanloup et al., 2004; Jing et al., 2012). The value of 5 km/s as P-wave velocity in the lunar core seems to be appropriate.

4.2. Seismic moment

For future lunar seismic experiments, the deep moonquakes will be the main targets, because the events repeatedly occur on identical sources, and some nests are already located from analysis of Apollo data (Nakamura, 2005). The located deep moonquake nests are useful in considering positions of the seismic stations to detect the lunar core-phase. In this study, we derive seismic moments of the events originated from the located active deep moonquake nests and use them for the evaluation of Eqs. (4) and (16).

4.2.1. Derivation of seismic moment

The seismic moment of a large deep moonquake (originated at 6:34, day 304, 1975) only was evaluated in Goins et al., (1981), but the deep moonquakes of the same nest have various amplitudes; suggesting variations of the seismic moments. Since we do not know this variation, we derived the distribution of the moment from the deep moonquake events observed by the Apollo LP. As described in Section 3.2, around frequency of 1 Hz where seismic energies can be identified from Apollo data, we assume that average square amplitude of an input impulse is equivalent to that of a waveform whose time window is T_0 after arrival to the surface, and the Fourier amplitude of the observed signal is represented by theoretical equation including attenuation effect such as Eq. (14). Then, the seismic moment could be estimated.

$$M_0 = S_{obs}(f_0, \Delta_{obs}, S)/S(f_0, \Delta_{obs}, S, M_0 = 1) \tag{17}$$

where $S_{obs}(f_0, \Delta_{obs}, S)$ is the Fourier amplitude of an observed S-waveform of a deep moonquake at frequency f_0 and epicentral distance Δ_{obs} and $S(f_0, \Delta_{obs}, S, M_0 = 1)$ is the calculated one using Eq. (14) with the seismic moment $M_0 = 1$. We use data of S-waveforms to derive seismic moments because the S-waveforms can be identified from deep moonquakes more clearly than P-waveform. We also apply $f_0 = 1.0$ Hz as the dominant frequency of deep moonquake. The Fourier amplitude of the observed waveform is calculated by

$$S_{obs}(f_0, \Delta_{obs}, S) = \int_{-T_0/2}^{T_0/2} u(t, \Delta_{obs}, S)\exp(-2\pi i f_0 t)dt \tag{18}$$

where $u(t, \Delta_{obs}, S)$ is the observed deep moonquake waveform in time series after arrival of S-waveform. This equation indicates that the values of Fourier amplitude and seismic moment of a deep event vary with length of time window T_0. However, we do not know how long the seismic coda of a seismic phase due to the seismic scattering continues. (Goins et al., 1981) selected the time window of 27 min to cover entire seismic coda of direct S-waveform, but it may be too long because many refracted and reflected seismic phases will arrive into the seismic coda and energies of their later phases can be added to the previous ones. Therefore, we apply two cases, minimum and maximum cases, to derive seismic moments.

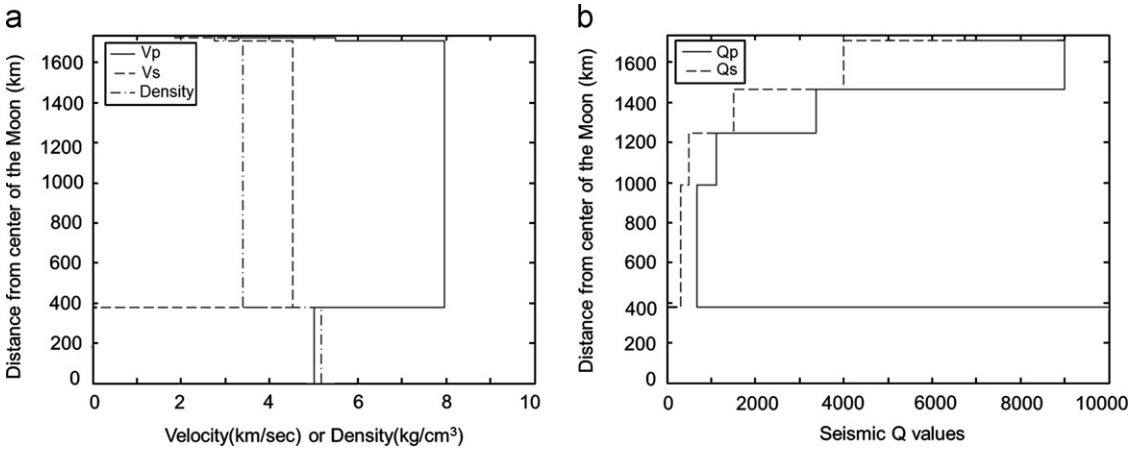

Fig. 7. Lunar interior model which has liquid Fe core whose size is 380 km; (a) profiles of P and S waveform velocities and density and (b) profiles of seismic quality factors of P and S waveform with radius of the Moon. These profiles are referred from VPREMOON model (Garcia et al., 2011).

In minimum case, we assume that seismic energy of direct S-waveform is preserved until other seismic phases arrive to the seismic station. This may be not necessarily correct; but it is conservative condition to evaluate the seismic moments. We assume that the S-waveform reflected at boundary between the surface low velocity zone and the upper crust is first seismic phase after arrival of direct S-waveform and reflection at lunar surface, though the reflected phases are not usually observed because they are buried in the seismic coda of direct S-waveform. The investigation of lunar surface structure (Cooper et al., 1974; Mark and Sutton, 1975; Vinnick et al., 2001) indicated the Moon had a low-velocity zone whose thickness was about 1 km at the surface and the averaged S-wave velocity was about 0.5 km/s. Though the arrival time of the reflected S-waveform depends on the reflected angle, first reflected wave will arrive at the seismometer in about 5 s later after arrival of direct S-waveform. We adopt $T_0=5.0$ s as the time window to evaluate seismic moment in the minimum case.

In maximum case, we apply the assumption in Goins et al. (1981). This paper estimated the Fourier amplitude of a deep moonquake from Apollo LP data whose length is 27 min. The waveforms of this time length roughly include overall envelope of the event and it is assumed that energy of direct S-wave is preserved over whole envelope and those of later reflected phases are negligible. We derive distributions of the seismic moment using $T_0=5.0$ s (minimum case) and $T_0=27$ min (maximum case) respectively, and evaluate detection of core-phases.

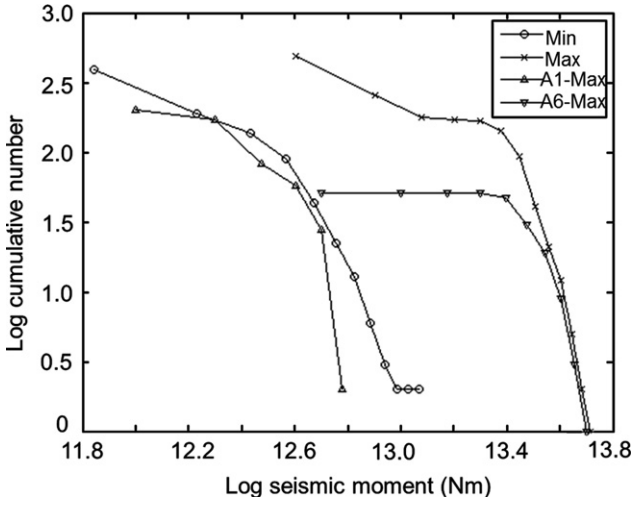

Fig. 8. Cumulative numbers of the deep moonquake events originated from active 15 nests which has seismic moment larger than a given value in both minimum and maximum seismic moment models. This figure also shows the cumulative numbers of deep events originated from specific nests; A1 and A6 related with seismic moment in only maximum case.

4.2.2. Locations of deep moonquakes

We describe the active nests of the deep moonquakes as target in the future missions. We define the active nests as those generating more than 50 identified events through period of Apollo seismic experiments and located with good accuracy in Nakamura (2005). The following 15 nests are selected; A1, A6, A7, A8, A9, A10, A13, A15, A18, A20, A21, A25, A33, A42 and A51. AX is the name of the deep moonquake nest defined in the Apollo long-period event catalog (Nakamura et al., 1981) and the locations are listed in Nakamura (2005). We derive a distribution of seismic moments through analysis of the Apollo deep moonquake events originating from these 15 nests.

4.2.3. Distribution of the seismic moments

About 800 deep events were analyzed to derive distributions of the seismic moments from the Fourier amplitude using Eqs. (17) and (18). These events have S/N large enough to identify arrival of S-waveform using the cross-correlation with reference stacking waveform (Nakamura, 2003). We used the seismic data observed at Apollo 12 LP for the analysis, because the seismic records at station 12 had equal amplitudes on all three components of ground motion and they are expected not to be affected by seismic polarization due to surface strong-scattering zone and indicate true amplitude (Goins et al., 1981). Then, Δ_{obs} in Eqs. (17) and (18) means epicentral distance between Apollo 12 seismic station and each active deep nest. Each seismic moment derived from one deep moonquake is the average moment of the three components data; two horizontal (LP*X* and LP*Y*) and one vertical (LP*Z*).

Fig. 8 shows the derived cumulative numbers of all analyzed deep events with seismic moments larger than a given value in minimum and maximum cases and those of two specific deep nest; A1 and A6 in only the maximum case, and Fig. 9 shows the occurrence number of the deep moonquake which has the seismic moment per year for each active deep nest with interval of 0.1 Nm in the (a) maximum case and (b) minimum case. These figures show that the activity and distribution of seismic moment are

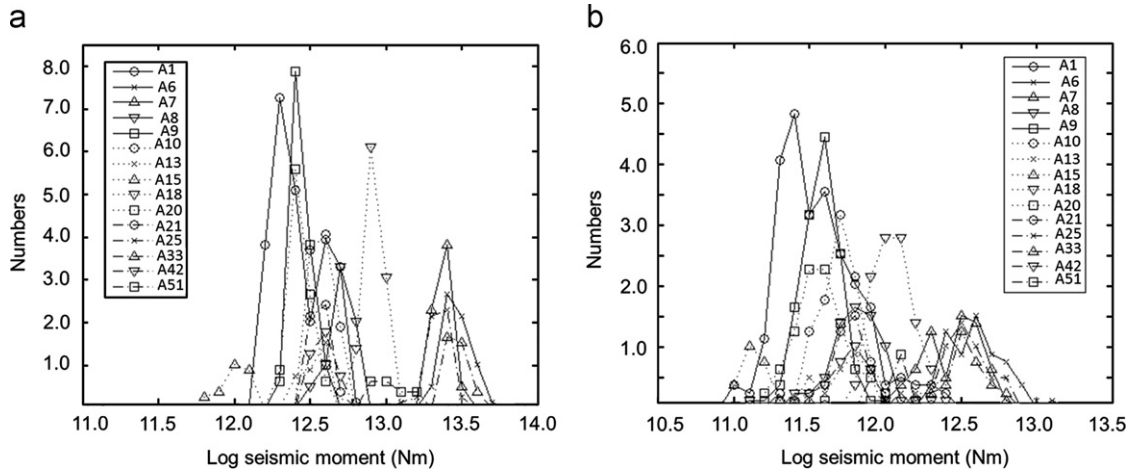

Fig. 9. Distribution of seismic moment of deep moonquake events of each active 15 nests in (a) maximum case and (b) minimum case. The number of event for each seismic moment is represented as number per year at intervals of 0.1 Nm in logarithmic expression.

different among each active deep nest. Then, we evaluate the possible numbers of core-phases to be detected by our seismometers during the observation period (one year) using seismic moment distribution for each active nest. One year is the expected observation term for future lunar missions such as the SELENE-2 mission. We also evaluate the detection number of core-phases originating from only the A1 nest, because A1 is the most active nest, as shown in Fig. 9, and it will be an important target for future experiments.

5. Results

In this section, we present the numbers of core-phases such as ScS and PKP expected to be detected by VBB and the SP through the one-year lunar mission. In Earth's case, a similar study was performed for teleseismic phases (Wysession, 1996). Fig. 10 shows the travel-time curves of five main seismic phases using the interior structure model shown in Fig. 7(a). In Fig. 10, PcP and ScS phases are P and S waveforms reflected at the core–mantle boundary. Here, we notice that the core-reflected waveforms such as PcP and ScS arrive as later phases of direct P and S waveforms, as shown in Fig. 10. Since these reflected phases are buried in intensive seismic coda of direct phases, we have to observe at low frequencies range where the effect of seismic scattering is weak. As described in Section 3, the VBB sensor is useful to achieve the observation at frequencies lower than 0.1 Hz. On the other hand, we will be able to detect PKP phase in high frequency range around 1.0 Hz on both the SP and the VBB, because PKP phase arrives first at large distances as shown in Fig. 10. For the VBB, we can also detect the PKP phase as later phase in low frequency range from 115 to 140° of epicentral distance shown in Fig. 10.

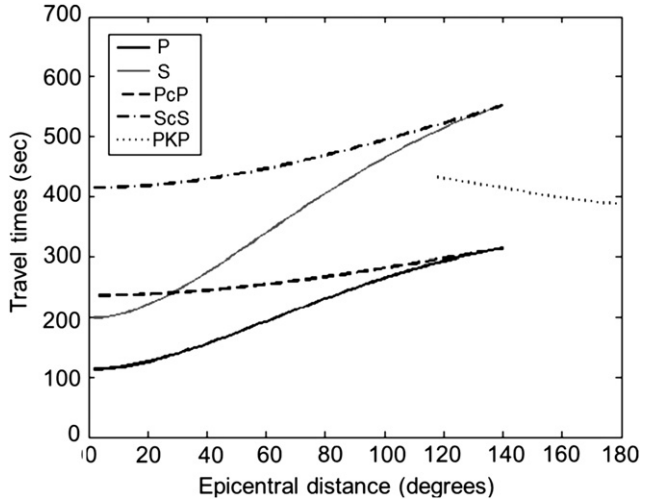

Fig. 10. Travel time curves of five seismic phases; P, S, PcP, ScS and PKP. These travel time curves were calculated using interior model shown in Fig. 7(a) and source depth of 867 km.

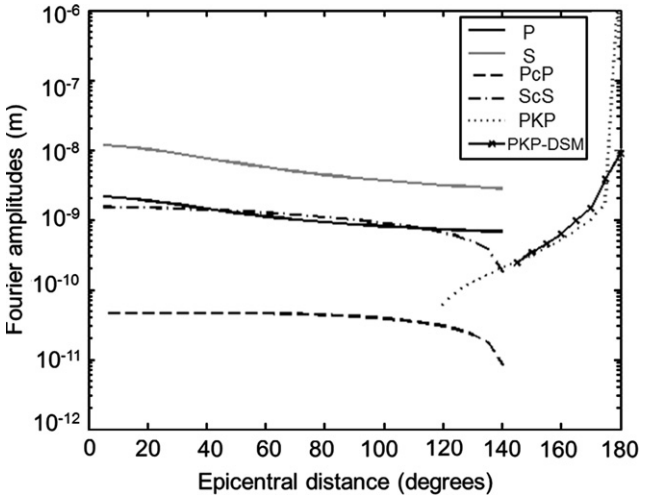

Fig. 11. Fourier amplitude of five seismic phases; P, S, PcP, ScS and PKP as function of epicentral distance at a frequency of 0.1 Hz. These amplitudes were calculated with seismic moment of 1.0E13 Nm using interior model shown in Fig. 7 and source depth of 867 km. 'PKP-DSM' means the amplitude of PKP phase calculated by Direct Solution Method (DSM).

Since the liquid core is more plausible than the solid core as described above, most energies of S-waveform can be reflected at the core–mantle boundary (Garcia et al., 2011). Fig. 11 indicates Fourier amplitudes of five seismic phases as a function of epicentral distance at frequency of 0.1 Hz. These amplitudes are calculated using Eq. (14) with seismic moment of 1.0E13 Nm. This figure shows that amplitude of ScS phase is about ten times larger than that of PcP phase under assumption of liquid core. From this reason, ScS phase will be the main core phase for the VBB sensor in future missions, and we evaluate the detection numbers of ScS phases and PKP phases for the VBB sensor. For the SP sensor, it is difficult to detect reflected core phases such as ScS phase or secondary PKP phase. However, first arrival PKP phase at large distances are expected to be detected by the SP sensor. We evaluate the detection numbers of PKP phases for both the SP and VBB sensor in this study.

On the other hand, the calculation of the amplitude of PKP phase using simple ray theoretical method such as Eq. (5) is not necessarily appropriate near focusing distance because it does not precisely represent effects of interference among various PKP phases arrive from various directions in lunar sub-surface structure. We, therefore, calculated amplitude of PKP phase with seismic moment of 1.0E+13 at far distance using DSM (Direct Solution Method). The result is shown in Fig. 11 as "PKP-DSM". This figure show that both calculations indicate similar values of amplitudes, but the profiles are specially distinguishes at epicentral distances larger than 175°. From this comparison, we correct the amplitude of PKP phase using result of DSM calculation at epicentral distance larger than 175°. On the other hand, it is difficult to represent effects of the interference to calculate the amplitude of PKP phases precisely, because we do not know the heterogeneity in lunar sub-surface structure affects the interference. We may be able to investigate this effect from comparison between our current calculations and actual amplitudes of PKP phases observed in future lunar seismic experiments.

5.1. ScS detection

In this section, the numbers of ScS phases to be detected by the VBB through one-year missions is evaluated. As described in Section 3.1, we can express waveform of ScS phase using theoretical Eq. (5) in low frequency range. Fig. 12 shows the calculated ScS waveform with the VBB noise. The waveform is calculated with seismic moment of 1.0E12.5 Nm at an epicentral distance of 10° and depth of 867 km (the depth of A1 nest) and filtered between 0.09–0.11 Hz. The seismic moment of 1.0E12.5 Nm is most expected value from deep events, as shown from Fig. 9(a) in maximum case. This waveform is expressed including the response of the VBB seismometer system and compared to the VBB noise model with sampling rate of 100 Hz and 24 bits resolution. With a noise amplitude spectral density of about 8.3E–11 m/s/Hz$^{1/2}$ at 0.1 Hz (Fig. 4) and a LSB of about 0.7E–12 m/s/DU, we expect, from Eq. (10), a RMS noise of about 1.2E–11 m/s in the 0.02 Hz (from 0.09 to 0.11 Hz) bandwidth, which corresponds to about 17 DU. This will

generate a peak-to-peak noise about three times this value, which is plotted in Fig. 12. This figure also shows that we will be able to identify the ScS waveform with possible seismic moment near the active deep nests by standard waveform stacking.

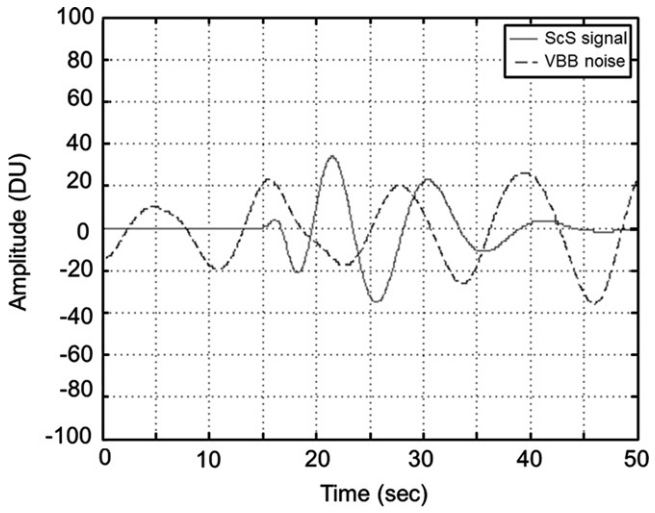

Fig. 12. Simulated ScS waveform of a deep moonquake observed by the VBB seismometer. The signal and noise are filtered between 0.09 and 0.11 Hz and simulated with sampling rate of 100 Hz and resolution of 24 bits. This event is assumed to be originated from a deep nest at epicentral distance of 40° and depth of 867 km with seismic moment of 1.0E12.5 Nm.

To evaluate detection numbers of core phases on each station position, we firstly derive M_{limit} using calculated U_{max} of ScS phases from all active 15 nests on the whole lunar surface (2° by 2°). It is defined as

$$M_{limit}(\theta,\varphi,A_i)=\frac{N_R}{U_{max}(\theta,\varphi,A_i,M=1)} \tag{19}$$

where θ is the latitude, φ is the longitude and A_i is the type of nest, as defined from 1 to 15. $U_{max}(\theta,\varphi,A_i,M=1)$ is the maximum amplitude of a core phase generated from nest A_i observed at a station position of (θ,φ), using a seismic moment of 1, and it is calculated from Eq. (5). Then, $M_{limit}(\theta,\varphi,A_i)$ is the minimum seismic moment at which we can detect core phases at the position of (θ,φ) for each deep nest A_i by the seismometer with RMS noise level of N_R. We can detect core phases which have seismic moment larger than M_{limit}. The value of M_{limit} is defined to be 0 if we cannot detect the core phases (ScS or PKP) outside observable distance range of the phases for each A_i nest. For example, we cannot observe ScS phases in far range larger than about 140°, as shown in Fig. 10.

Then, expected detection number of core phases per year (EXN) on each position is defined as below equation;

$$\mathrm{EXN}(\theta,\varphi)=\sum_{i=1}^{15}\mathrm{CDN}(A_i,M_{limit}(\theta,\varphi,A_i)) \tag{20}$$

where CDN is the cumulative number of deep moonquakes per year which has seismic moments larger than M_{limit} for each deep nest A_i. CDN is defined to be 0 when M_{limit} is 0 for each A_i. The value of CDN is derived from Fig. 9 in both maximum and

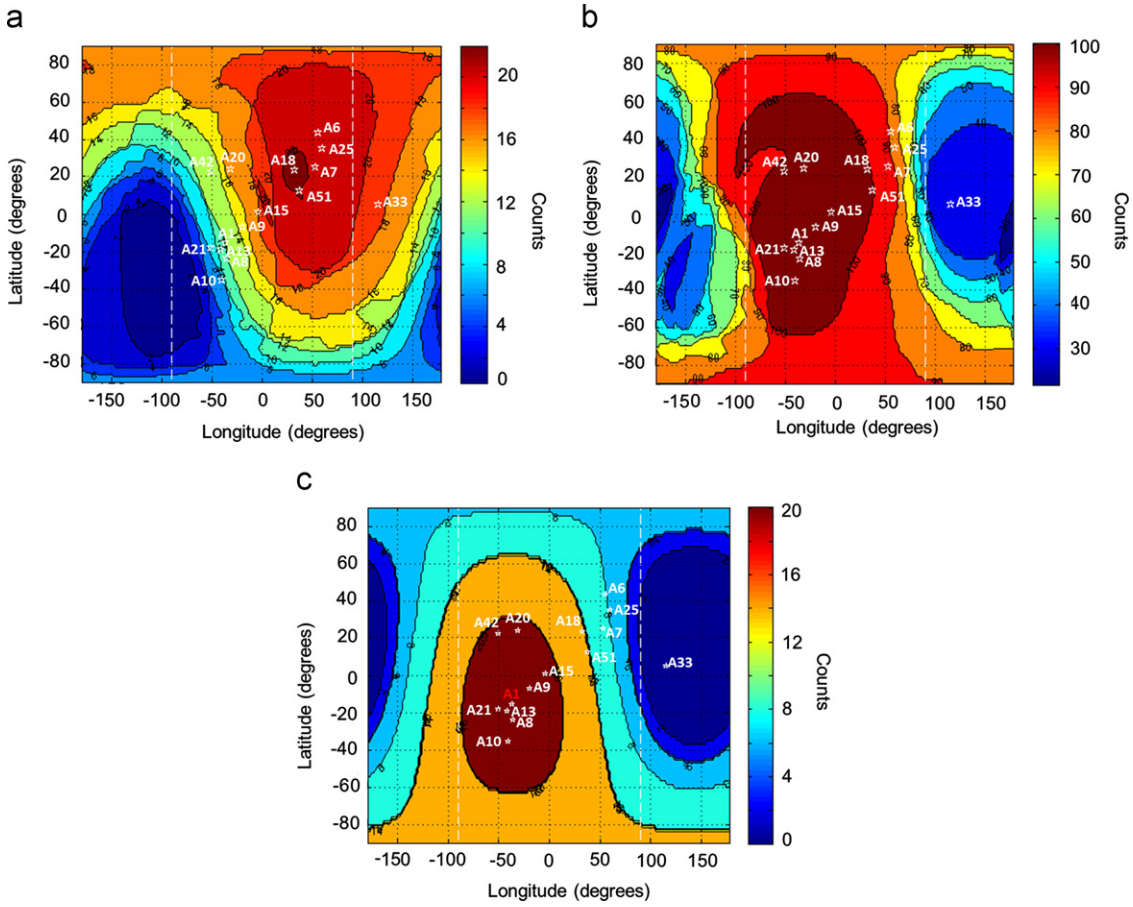

Fig. 13. The number of ScS phases expected to be detected by the VBB around 0.1 Hz from active 15 nests during one year mission using the (a) minimum and (b) maximum seismic moment models. These numbers are evaluated on each station position (2° by 2°) using lunar interior model shown in Fig. 7. The figure of (c) also indicates number of ScS phases to be detected by the VBB around 0.1 Hz from only A1 nest during same term under assumption of maximum seismic moment and seismic activity of A1.The white stars indicate the epicenters of active deep nests located in (Nakamura, 2005), and the white vertical dashed lines are boundaries between lunar near-side and far-side (lines of +90° and −90°).

minimum cases. We assume that active deep nests generate deep moonquakes following activities during Apollo-era as shown in Figs. 8 and 9 in future experiments.

Fig. 13 shows the values of EXN(θ,φ) of the ScS-phase to be detected by VBB on the lunar surface for the (a) minimum case and (b) maximum case. If we assume seismic moments as minimum case, we can expect detection of about 20 ScS phases around north-east region on the lunar near-side during one year. As shown in Fig. 9, since the active deep nests located in north-east region as A6 and A7 has larger seismic moments than other nests, deployment of a seismic station on the region will be desirable to detect the reflected core phases. On the other hand, if we assume seismic moments as maximum case, about 100 ScS phases per year may be detected on entire lunar nearside, mainly west side. In maximum case, we can detect ScS phases generated from more active nests such as A1, and deployment on west side around A1 site is more desirable. These figures show that desirable station positions to detect core reflected-phases are different depending on assumptions of seismic moment, though minimum case is more conservative condition. Common to both cases, the positions around A18 and A51 may be good place to detect ScS phase, and then we could detect about 20–100 ScS phases around the region. Anyway, in the plan of SELENE-2 mission, the soft-landers will be deployed on lunar near-side for direct communication to the Earth. Use of the VBB sensor will be gainful to detect ScS phases in this mission.

On the other hand, Fig. 13(c) shows EXN(θ,φ) of the ScS phase for only the most active nest; A1 in the maximum case. In this result, we use only CDN and M_{limit} of A1 in the calculation of EXN. We can expect about 20 ScS phases will be detected aroundA1 nest. Deployment of the seismic station on south-west region of lunar near-side will be efficient to detect ScS phases from the A1nest.

5.2. PKP detection

We show the results for PKP detection using the VBB sensor. Fig. 14 indicate the values of EXN(θ,φ) of PKP-phase to be detected by the VBB on lunar surface for the (a) minimum case, (b) maximum case and (c) A1 maximum case. These results were also calculated using Eqs. (19) and (20) for PKP phase around frequency range of 0.1 Hz [0.09–0.11 Hz]. As described in previous section, we corrected values of U_{max} at epicentral distances larger than 175° using results of DSM. On the other hand, this correction does not change number of PKP detection so much because the epicentral distance larger than 175° are about 1–2% among all calculated distances.

Fig. 14(a) indicates that we can detect about 15 PKP phases per year at south-west region of lunar far-side where are corresponding to antipodes of active deep nests located in north-east region of the lunar near-side. In maximum case (Fig. 14(b)), we may be able to detect about 40 PKP phases in north-east region of lunar far-side where are corresponding to antipodes of the deep nests located in south-west region of the lunar near-side as much as the south-west region of lunar far-side. In the case, the south-west region of lunar near-side will be also targeted place for deployment of the seismic

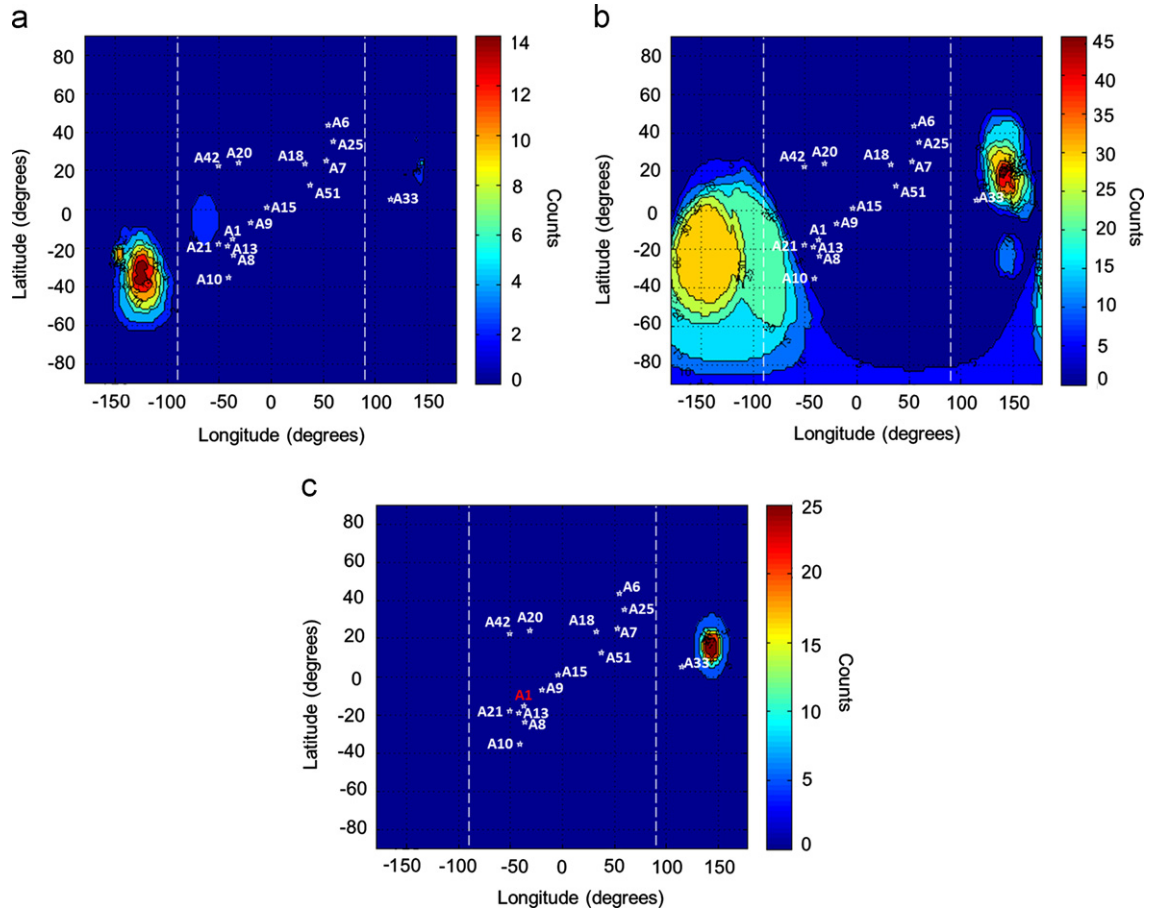

Fig. 14. Number of PKP phases expected to be detected by the VBB around 0.1 Hz from active 15 nests during 1 year mission using the (a) minimum and (b) maximum seismic moment models. These numbers are evaluated on each station position (2° by 2°) using lunar interior model shown in Fig. 7. The figure of (c) also indicates number of PKP phases to be detected by the VBB around 0.1 Hz from only A1 nest during same term under assumption of maximum seismic moment and seismic activity of A1. The white stars indicate the epicenters of active deep nests located in (Nakamura, 2005), and the white vertical dashed lines are boundaries between lunar near-side and far-side (lines of +90° and −90°).

station. Fig. 14(c) indicates expectation of detection of about 25 PKP phases from the A1 nest around antipode of A1 in maximum case. These are almost first arrival seismic phases and can be detected not only at low frequencies but also at high frequencies.

The SP sensor is also available to detect first arrival PKP phases in far epicentral distance region. To derive EXN of the SP sensor in high frequency range, we calculate M_{limit} using next equation;

$$M_{limit}(\theta,\varphi,A_i)=\frac{\overline{nw}^2}{\overline{sw}^2(\theta,\varphi,A_i,M=1)} \tag{21}$$

where $\overline{nw}^2(\theta,\varphi,A_i,M=1)$ is average square amplitude of moonquake waveform generated from deep nest A_i at station position of (θ,φ) and it is calculated from Eqs. (12)–(14) using seismic moment of 1.

Fig. 15 shows the EXN(θ,φ) of first arrival PKP-phase to be detected by the SP for the (a) minimum and (b) maximum seismic moment models derived from Eq. (20) using M_{limit} in Eq. (21). Fig. 15(a) shows that we could detect about 10 PKP phases on south-west region of lunar far-side. This region corresponding to antipode of deep nests occur large moment events such as A6 and A7. In the maximum case, we could also detect about 5 PKP phases on south-west limited region of the lunar far-side as shown in Fig. 15(b). The reason which the EXN(θ,φ) is less in the maximum case than those in the minimum case is caused from calculation of the average square amplitude in the Eqs. (12) and (13). In this equation, we divide the Fourier amplitude by the time window of T_0 to represent the average square amplitude. $T_0=1620$ s (27 min) may be too long as time window to represent seismic energy. Anyway, the deployment of the seismic stations on south-west region of lunar far-side will be important to detect PKP phases for both the SP and the VBB.

However, in the case of the SELENE-2 mission, the deployment in the lunar far-side is not planned. The deployment of the seismic station in the lunar far-side will be expected for Farside explorer and future penetrator missions such as past LUNAR-A project. Since the SP sensor can be implemented on the penetrator, the sensor is useful to detect seismic phase which pass through interior of the core, assuming of course that the source reference time is constrained by a seismic measurement on the near side. This will therefore enable cost optimization for future seismic networks, for example if based on a single SELENE-2 lander complemented with several penetrators and might better address seismic constraints on lunar lateral variations (Chenet et al., 2006).

Due to its focus on core phases, we have concentrated our discussion in the 0.1–1.5 Hz bandwidth, but other signals will be recorded below 0.1 and above 1.5 Hz. For example, the SP sensor on soft-landers can record signal up until 50 Hz, which will allow the detection of high frequency lunar seismic events, such as shallow moonquakes (Nakamura, 1977), small and regional meteoroid impact and thermal moonquakes (Diennebier and Sutton, 1974b), in addition to the investigation of the source functions of their events including the deep moonquakes. On the low frequency end, although free oscillations observations will be likely only for operation duration comparable to Apollo (Gudkova and Zharkov, 2002; Lognonné, 2005), surface waves are likely to be detected by the VBB below 0.1 Hz (Gagnepain-Beyneix et al., 2006).

6. Discussion

6.1. Source parameters of deep moonquake

In this study, we have calculated the seismic moments of deep moonquakes from Fourier amplitude spectrum in two cases of time window. As shown in Fig. 8, the distributions of the seismic moments of deep moonquakes are largely different between the two assumptions. From the reason, we derived the expected detection numbers of core-phases both in two end cases. We can say at least that we can expect the detection numbers in range of results between minimum and maximum cases as shown in Figs. 13–15. For sure detection, we recommend to refer maps of the minimum case such as Figs. 13(a) and 14(a) and the maximum case as Fig. 15(b), because they are severer conditions.

We also assumed a radiation pattern of 0.5 for all seismic phases. We do not have distinct information of radiation pattern of the deep moonquake, though some focal mechanisms are estimated (Nakamura, 1978; Weber et al., 2009). The value of the radiation pattern changes values of the seismic moment shown in Figs. 8 and 9 from calculation of Eq. (17). But that may not affect the calculation of Fourier amplitude from Eqs. (7), (9) and (14), because effects of radiation pattern cancel out in the calculation of $S(f,\Delta,K)$ under assumption of constant radiation pattern.

6.2. Lunar interior model

In this study, we used a lunar interior model which has constant velocity in the mantle based on VPREMOON model (Garcia et al.,

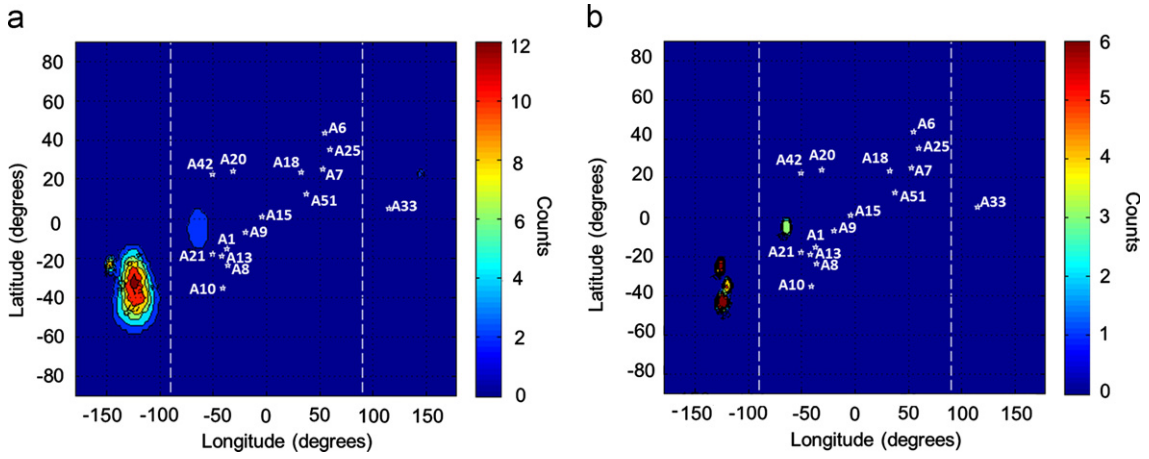

Fig. 15. Number of PKP phases expected to be detected as first seismic arrival phase by the SP around 1.0 Hz (from 0.5 to 1.5 Hz) during one year mission using the (a) minimum and (b) maximum seismic moment models. These numbers are evaluated on each station position (2° by 2°) using lunar interior model shown in Fig. 7. The white stars indicate the epicenters of active deep nests located in (Nakamura, 2005), and white vertical dashed lines are boundaries between lunar near-side and far-side (lines of +90° and −90°).

2011). However, there are two cases of researches which describe that lunar mantle has boundaries where the velocities change (Goins et al., 1978; Nakamura, 1983) or constant velocity (Khan et al., 2006). Though we do not have credible evidence of the boundaries, the velocity change of a few percent in the mantle does not vary the amplitudes of core-phases so much.

On the other hand, the value of seismic quality factor (attenuation parameter) varies the amplitudes of core-phases much more than the velocity. The seismic quality factors were derived from analysis of amplitudes and power spectra of lunar seismic events (Nakamura et al., 1976; Nakamura and Koyama, 1982), and the values have large errors especially in the deep Moon. We will need further analysis of Apollo seismic data and/or new seismic data observed by broad band seismometer to constrain the attenuation parameters with better accuracy.

The lunar sub-surface structure has also an important effect on amplitudes. In this study, even if we ignored seismic amplification caused from surface fractured structure, the structures will differ depending on location of seismic station and may change the amplitudes of core-phases at different landing sites. Though we cannot apply this effect to our calculation accurately, because we do not know the lunar sub-surface structures except for some Apollo landing sites, comparison of the calculated amplitudes of seismic phases in this study with actual amplitudes observed in future missions could give information of the sub-surface structure and interference among seismic phases of the landing site.

1. Conclusion

In this study, we evaluated detection capabilities of the seismic phases which are reflected from core-mantle boundary and pass through interior of the core by the new seismometers for soft-landers in future lunar missions. First, we confirmed that we can observe the lunar seismic events with a much better S/N compared with past Apollo seismometers using expected performance of the new seismometers. Then, we evaluated the number of core-phases to be detected during future missions in low frequency range for ScS and PKP by the VBB and high frequency range for PKP by the SP following distributions of seismic moments of deep moonquakes under two assumptions.

Referring to recent lunar interior model (Garcia et al., 2011), we expect that the VBB can detect ScS and PKP phases around 0.1 Hz where effect of scattering will weaken in seismic coda. The expected detection numbers of ScS phase originated from 15 active deep moonquake nests are about 100 on west side of lunar near-side in maximum case and about 20 on north-east side of lunar near-side in minimum case during one year observation. The detection of about 5–10 PKP phases by the SP and 15–30 by the VBB can be also expected at south-west region of lunar far-side during one year, and limited regions in southern-west region of lunar near-side may be also appropriate place to detect PKP phases for only the VBB

We still have uncertainties about source parameters of deep moonquakes, lunar seismic quality factor and lunar sub-surface structures. Though changes in these parameters would vary results of detection numbers, the positions to detect the core-phases may essentially not change because they are mainly governed by the geometry of deep nest locations. Then, the contour maps such as Figs. 13–15 will be gainful to plan the positions of seismic stations in future lunar seismic experiments. From this study, we demonstrate that the seismometers of lunar soft-landers have performances allowing to observe direct waveforms more clearly than past Apollo mission and to detect core-phases. If we select appropriate locations of the seismic stations following our results, we can obtain very important data so as to constrain lunar core parameters (size, state and composition), and better understand origin and evolution of the Moon.

References

Aki, K., Richards, P.G., 2002. Body waves in media with depth-dependent properties. In: Ellis, J. (Ed.), Quantitative Seismology, second edition University Science Books, California, pp. 385–490.

Canup, R.M., Asphaug, E., 2001. Origin of the Moon in a giant impact near the end of the Earth's formation. Nature 412, 708–712.

Chenet, H., Lognonné, P., Wieczorek, M., Mizutani, H., 2006. Lateral variations of lunar crustal thickness from Apollo seismic dataset. Earth and Planetary Science Letters 243, 1–14.

Cooper, M.R., Kovach, R.L., Watkins, J.S., 1974. Luna near-surface structure. Reviews of Geophysics and Space Physics 12 (3), 291–308.

Dainty, A.M., Toksöz, M.N., Anderson, K.R., Pines, P., 1974. Seismic scattering and shallow structure of the Moon in Oceanus Procellarum. The Moon 9, 11–29.

Duennebier, F., Sutton, G.H., 1974A. Meteoroid impacts recorded by the short-period component of Apollo 14 lunar passive seismic station. Journal of Geophysical Research 79 (29), 4365–4374.

Duennebier, F., Sutton, G.H., 1974B. Thermal moonquakes. Journal of Geophysical Research. 79 (29), 4351–4363.

Gagnepain-Beyneix, J., Lognonné, P., Chenet, H., Lombardi, D., Sphon, T., 2006. A seismic model of the lunar mantle and constraints on temperature and mineralogy. Physics of the Earth and Planetary Interiors 159, 140–166.

Garcia, R.F., Gagnepain-Beyneix, J., Chevrot, S., Lognonné, P., 2011. Very preliminary reference Moon model. Physics of the Earth and Planetary Interiors 188, 96–113.

Goins, N.R., ToksÖz, M.N., Dainty, A.M., 1978. Seismic structure of the lunar mantle: an overview. In: Proceedings of the 9th Lunar Planetary Science Conference. pp. 3575–3588.

Goins, N.R., Dainty, A.M., Toksöz, M.N., 1981. Seismic energy release of the Moon. Journal of Geophysical Research 86 (B1), 387–388.

Gudkova, T.V., Zharkov, V.N., 2002. The exploration of the lunar interior using torsional oscillations. Planetary and Space Science 50, 1037–1048.

Hood, L.L., Mitchell, D.L., Lin, R.P., Acuna, M.H., Binder, A.B., 1999. Initial measurements of the lunar induced magnetic dipole moment using lunar prospector magnetometer data. Geophysical Research Letters 26, 2327–2330.

Jing, Z., Wang, Y., Yu, T., Sakamaki, T., Kono, Y., Park, C., 2012. In-situ ultrasonic sound velocity measurements of Fe and Fe-light element alloying liquids at high pressures with implications to planetary cores. In: Proceedings of the American Geophysical Union, Fall Meeting. (Abstract) #DI33A-2426.

Khan, A., Mosegaard, K., 2005. Further constraints on the deep lunar interior. Geophysical Research Letters 32, L22203, http://dx.doi.org/10.1029/2005GL023985.

Khan, A., Maclennan, J., Taylor, S., Connolly, J., 2006. Are the Earth and the Moon compositionally alike? Inferences on lunar composition and implications for lunar origin and evolution from geophysical modeling. Journal of Geophysical Research 111, E05005, http://dx.doi.org/10.1029/2005JE002608.

Kim, W.J., Sushkov, A.O., Dalvit, D.A.R., Lamoreaux, S.K., 2010. Surface contact potential patches and Casimir force measurements. Quantum Physics arXiv 0905, 3421v3.

Lammlein, D.R., 1977. Lunar seismicity and tectonics. Physics of the Earth and Planetary Interiors 14, 224–273.

Latham, G., Ewing, M., Dorman, J., Nakamura, Y., Press, F., Toksöz, N., Sutton, G., Duennebier, F., Lammlein, D., 1973. Lunar structure and dynamics: results from Apollo Passive Seismic Experiment. The Moon 7, 396–420.

Lognonné, P., Gagnepain-Beyneix, Banerdt, W.B., Cacho, S., Karczewski, J.F., Morand, M., 1996. An ultra-broad seismometer on InterMarsnet. Planetary and Space Sciences 44, 1237–1249.

Lognonné, P., Giardini, D., Banerdt,, B., et al., 2000. The NetLander very broad band seismometer. Planetary and Space Science 48, 1289–1302.

Lognonné, P., Gagnepain-Beyneix, J., Chenet, H., 2003. A new seismic model of the Moon: implications for structure, thermal evaluation and formation of the Moon. Earth and Planetary Science Letters 211, 27–44.

Lognonné, P., 2005. Planetary Seismology. Annual Review of Earth and Planetary Science 33191-19.34, http://dx.doi.org/10.1146/annurev.earth.33.092203.122605.

Lognonné, P., Johnson, C., 2007. Planetary seismology, in treatise in geophysics. In: Shubert, G. (Ed.), Planets and Moons, 10. Elsevier, pp. 69–122.

Lognonné, P., Le Feuvre, M., Johnson, C.L., Weber, R.C., 2009. Moon meteoritic seismic hum: steady state prediction. Journal of Geophysical Research 114, E12003, http://dx.doi.org/10.1029/2008JE003294.

Mark, N., Sutton, G.H., 1975. Lunar shear velocity structure at Apollo Site 12, 14 and 15. Journal of Geophysical Research 80 (35), 4932–4938.

Mimoun, D., Wieczorek, M., Alkalai, L., et al., 2011. Farside explorer: unique science from a mission to the farside of the moon. Experimental Astronomy, 10.1007/s10686-011-9252-3.

Mizutani, H., Fujimura, A., Tanaka, S., Shiraishi, H., Nakajima, T., 2003. LUNAR-A MISSION: goals and status. Advances in Space Research 31, 2315–2321.

Nakamura, Y., Duennebier, F., Latham, G., Dorman, J., 1976. Structure of the lunar mantle. Journal of Geophysical Research. 81 (26), 4818–4824.

Nakamura, Y., 1977. HFT events: shallow moonquakes. Physics of the Earth and Planetary Interiors 14, 217–223.

Nakamura, Y., 1978. A1 moonquakes: source distribution and mechanism. In: Proceedings of Lunar and Planetary Science Conference Proceeding 9. pp. 3589–3607.
Nakamura, Y., Latham, G., Dorman, J., Harris, J., 1981. Passive seismic experiment long-period event catalog. Galveston Geophysics Laboratory Contribution, 491.
Nakamura, Y., Koyama, J., 1982. Seismic Q of the lunar upper mantle. Journal of Geophysical Research 86 (B6), 4855–4861.
Nakamura, Y., Latham, G.V., Dorman, H.J., 1982. Lunar seismic experiment: final summary-. Journal of Geophysical Research. 87, A117–A123. (Suppl.).
Nakamura, Y., 1983. Seismic velocity structure of the lunar mantle. Journal of Geophysical Research. 88 (B1), 677–686.
Nakamura, Y., 2003. New identification of deep moonquakes in the Apollo lunar seismic data. Physics of the Earth and Planetary Interiors 139, 197–205.
Nakamura, Y., 2005. Farside deep moonquakes and deep interior of the Moon. Journal of Geophysical Research 110, E1001, http://dx.doi.org/10.1029/2004JE002322.
Neal, C.R., Banerdt, W.B., Alkalai, L., 2010. LUNETTE: establishing a lunar geophysical network without nuclear power through a discovery-class mission. In: Proceedings of the 41st Lunar and Planetary Science Conference (Abstract). 2710.
Ogawa, K., Iijima, Y., Tanaka, S., 2010. Thermal control unit for long-time survival of scientific instruments on lunar surface. 38th COSPAR Scientific Assembly. (Abstract), B01.
Rodgers, W.,P., 1992. Frequency limits for seismometers as determined from signal to noise ratios. Part.1: the electromagnetic seismometer. Bulletin of the Seismological Society of America 82 (2), 1071–1098.
Sanloup, C., Fiquet, G., Gregoryanz, E., Morard, G., Mezouar, M., 2004. Effect of Si on liquid Fe compressibility: implications for sound velocity in core materials. Geophysical Research Letters 31, L07604, http://dx.doi.org/10.1029/2004GL019526.
Sellers, C.,P., 1992. Seismic evidence for a low-velocity lunar core. Journal of Geophysical Research 97 (E7), 11663–11672.
Shiraishi, H., Kobayashi, N., Takeuchi, N., Murakami, H., Lognonné, P., et al., 2010. Lunar broadband seismometer system in the Japanese lunar landing mission SELENE-2; its science goals and instrument details. In: Proceedings of the American Geophysical Union, Fall Meeting (Abstract). #U51B-0039.
Tanaka, S., Shiraishi, H., Kato, M., Okada, T., 2008. group of Post SELENE missions. Advances in Space Research 42, 394–401.
Vinnick, L., Chenet, H., Gagnepain-Beyneix, J., Lognonné, P., 2001. First seismic receiver functions on the Moon. Geophysical Research Letters 28, 3031–3034.
Weber, R.C., Gills, B.G., Johnson, C.L., 2009. Constraints on deep moonquake focal mechanism through analysis of tidal stress. Journal of Geophysical Research 114, E05001, http://dx.doi.org/10.1029/2008JE003826.
Weber, R., Lin, P., Garnero, E., Williams, Q., Lognonné, P., 2011. Seismic detection of the lunar core. Science 311, 309–312.
Wieczorek, A., M., Jolliff, L., B., Khan, A., et al., 2006. The constitution and structure of the lunar interior. In: Rosso, J. (Ed.), Reviews in Mineralogy and Geochemistry, 60. The Mineralogical Society of America, Virginia, pp. 221–364.
Williams, J.G., Boggs, D.H., Yoder, C.F., Ratcliff, J.T., Dicley, J.O., 2001. Lunar rotational dissipation in solid body and molten core. Journal of Geophysical Research 106, 27933–27968.
Wysession, E.M., 1996. How well do we utilize global seismicity? BBSA 86 (5), 1207–1219.
Yamada, R., Yamada, I., Shiraishi, H., Tanaka, S., Takagi, Y., Kobayashi, N., Takeuchi, N., Ishihara, Y., Murakami, H., Yomogida, K., Koyama, J., Fujimura, A., Mizutani, H., 2009. Capability of the penetrator seismometer system for lunar seismic event observation. Planetary and Space Science 57, 751–763.
Yamada, R., Shiraishi, H., Tanaka, S., Fujimura, A., Yamada, I., Araya, A., Kobayashi, N., Nébut, T., Mimoun, D., Lognonné, P., 2010. Improvement of the seismometer developed for the LUNAR-A penetrator. 38th COSPAR Scientific Assembly. (Abstract), B01.